Acta Oceanol. Sin., 2025, Vol. 44, No. 3, P. 117–129
https://doi.org/10.1007/s13131-025-2475-3

Dynamics and energetics of semidiurnal internal tides in the Weddell-Scotia Confluence

Wenjia Min[1, 3], Qun Li[2*], Zhiliang Liu[1, 3], Bo Zhao[1, 3], Yue Ma[1, 3], Hang Chang[4], Weidong Wang[5, 6]

[1] Research Center for Marine Science, Hebei Normal University of Science and Technology, Qinhuangdao 066004, China
[2] MNR Key Laboratory for Polar Science, Polar Research Institute of China, Shanghai 200136, China
[3] Hebei Key Laboratory of Ocean Dynamics, Resources and Environments, Qinhuangdao 066004, China
[4] School of Science, Jimei University, Xiamen 361021, China
[5] National Marine Data and Information Service, Ministry of Natural Resources, Tianjin 300171, China
[6] Observation and Research Station of Bohai-rim Sea Level Change and Coastal Erosion, Ministry of Natural Resources, Tianjin 300171, China

Received 8 October 2024; accepted 24 March 2025
© Chinese Society for Oceanography and Springer-Verlag GmbH Germany, part of Springer Nature 2025

Abstract

We use a high-resolution numerical simulation to analyze the generation and evolution of semidiurnal internal tides in the Weddell-Scotia Confluence. Our results indicate that two ridges near the Antarctic Peninsula, the South Scotia Ridge (SSR) and the Philip Ridge (PR), are energetic sources of semidiurnal internal tides. The strongest semidiurnal barotropic to baroclinic energy conversion occurs around the crest of the SSR, reaching 0.3 W/m^2. The depth-integrated, tidally averaged semidiurnal internal tide energy fluxes that radiated from the SSR reach about 2 kW/m. The northward semidiurnal internal tide energy fluxes entering the Scotia Sea are stronger than the southward energy fluxes entering the Powell Basin. For the SSR region between the South Orkney Plateau and Elephant Island, the area-integrated barotropic to baroclinic conversion rate is 0.71 GW, of which 0.56 GW (79%) dissipates locally. The dissipation of internal tides occurs mainly in water depths of less than 1 000 m. The dissipation rate over the SSR is as high as 10^{-7} W/kg. The energy fluxes create an anticlockwise gyre between the SSR and PR. The horizontal kinetic energy and available potential energy oscillate sinusoidally with peaks occurring at quarter-wavelength intervals. This energy pattern suggests the formation of standing waves due to interference between the semidiurnal internal tides originating from the SSR and PR. The results of this study show that internal tides and related mixing need to be considered in the analysis of water mass transformation in the Southern Ocean.

Key words internal tides, Weddell-Scotia Confluence, standing waves, MITgcm

Citation Min Wenjia, Li Qun, Liu Zhiliang, Zhao Bo, Ma Yue, Chang Hang, Wang Weidong. 2025. Dynamics and energetics of semidiurnal internal tides in the Weddell-Scotia Confluence. Acta Oceanologica Sinica, 44(3): 117–129, doi: 10.1007/s13131-025-2475-3

1 Introduction

Internal tides generated by barotropic tidal motions over topography features (e.g., shelf breaks, ridges, mountains, and canyons) are broadly distributed over the world's oceans (Kerry et al., 2013; Vlasenko et al., 2014; Alford et al., 2015; Zhao et al., 2016; Min et al., 2023). These internal tides can propagate thousands of kilometers before they dissipate (Zhao et al., 2016; Zaron, 2019). Low-mode internal waves can propagate long distances (Zhao et al., 2016), while high-mode waves tend to dissipate near their generation site (St Laurent and Nash, 2004;

Foundation item: The Doctor Foundation of Hebei Normal University of Science and Technology under contract No. 2024YB039; the Fundamental Research Funds for the Provincial Universities of Hebei under contract Nos 2023JK07 and 2022JK03; the Major Science and Technology Support Project of Hebei Province under contract No. 242S3301Z; the Fujian Provincial Natural Science Foundation of China under contract No. 2021J05172; the National Natural Science Foundation of China under contract No. 42176244; the CAS Key Deployment Project of Centre for Ocean Mega-Research of Science under contract No. COMS2020Q07.
*Corresponding author, E-mail: liqun@pric.org.cn

Klymak et al., 2008). The breaking of internal tides contributes considerably to diapycnal mixing in the world ocean (Waterhouse et al., 2014; Wang et al., 2016; MacKinnon et al., 2017). Quantifying where and how internal tides dissipate is vital to understanding oceanic tidal energy transfer.

The South Scotia Ridge (SSR), northeast of the Antarctic Peninsula, separates the Scotia Sea from the Weddell Sea (Fig. 1). It has complex topography. The SSR is an important gateway for dense water of the Weddell Sea to enter the Scotia Sea and ultimately the global ocean, playing a notable role in global meridional overturning circulation (Naveira Garabato et al., 2002; Meredith et al., 2015).

The Weddell-Scotia Confluence lies poleward of the critical latitude at which the tidal constituent frequency (ω) matches the local inertial frequency (f) for diurnal tides. Therefore, freely propagating diurnal internal tides cannot be generated. However, semidiurnal internal tides can occur, radiating out from the Weddell-Scotia Confluence. Semidiurnal barotropic tidal currents, which can reach tens of centimeters per second (Robertson et al., 1985), are an important component of the total velocity field over the SSR region. Barotropic tidal currents affect mass exchange (Zhou et al., 2020) and the Antarctic Ice Sheet (Padman et al., 2018). Interaction of the barotropic tidal currents with the SSR results in the formation of internal tides. These internal tides can affect large-scale ocean circulation, transport of nutrients and momentum (Bennetts et al., 2024). Besides, the internal tides can in-

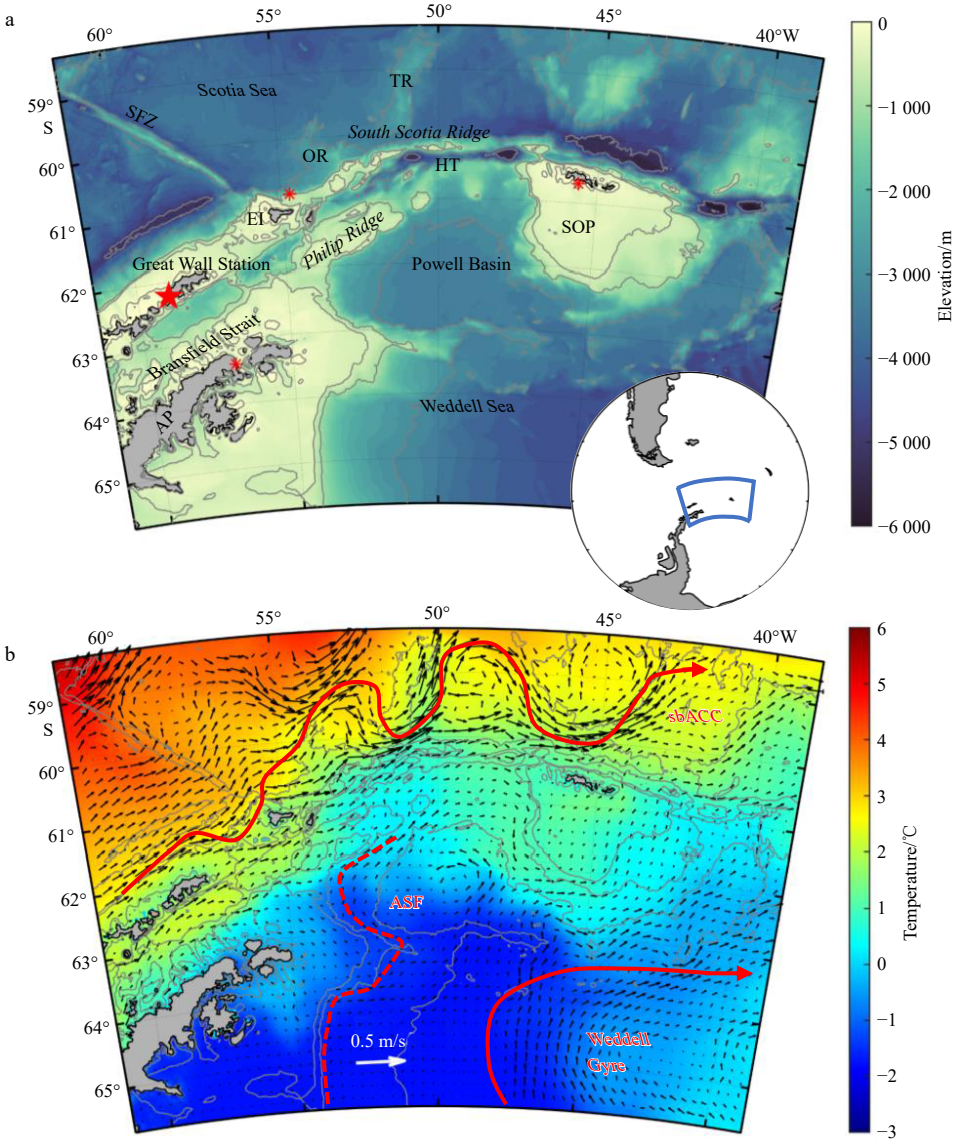


Fig. 1. Bathymetry of the model domain (a), and sea surface subtidal currents (black arrows) and sea surface temperature (colors) (b). The three red asterisks in a indicate the positions of the tide gauges. Bathymetry contours at −100 m, −500 m, −1 000 m, −3 000 m, −5 000 m. AP: Antarctic Peninsula; SOP: South Orkney Plateau; HT: Hesperides Trough; TR: Terror Rise; OR: Ona Rise; EI: Elephant Island; SFZ: Shackleton Fracture Zone; sbACC: southern boundary of the Antarctic Circumpolar Current; ASF: Antarctic Slope Front.

fluence the local turbulent mixing when they impinge on steep topography (Guo et al., 2016).

Previous studies have shown that the Weddell-Scotia Confluence is a hotspot of semidiurnal internal tides (Simmons et al., 2004; Robertson, 2005; Padman et al., 2006; Heywood et al., 2007; Buijsman et al., 2020). A global simulation by Simmons et al. (2004) indicated that the SSR is an important source of M_2 internal tides. The depth-integrated, time-averaged energy fluxes can reach as high as about 10 kW/m. However, Padman et al. (2006) suggested that the SSR energy fluxes of Simmons et al. (2004) may be overestimated, and the energy is sensitive to grid resolution and stratification. Note that both studies above were based on horizontal homogeneous stratification, which cannot accurately characterize the complexity of regional stratification. Therefore, the dynamics and energetics of internal tides in the Weddell-Scotia Confluence merit further investigation.

Internal tides from different source sites will interfere with each other, creating complex interference patterns (Kelly and Nash, 2010; Rainville et al., 2010; Nash et al., 2012; Kerry et al., 2013; Buijsman et al., 2014; Wang et al., 2018, 2021). Under the right conditions standing waves may form (Buijsman et al., 2014). In the Luzon Strait, internal tides generated from two parallel ridges create a standing wave pattern with their interference (Buijsman et al., 2014). The formation of standing waves could lead to enhanced dissipation (Waterhouse et al., 2014; Hamann et al., 2021). The area of the Weddell-Scotia Confluence includes topographic features similar to those in the Luzon Strait. Whether standing waves are formed and how the dissipation of internal tides distributes are intriguing problems that need to be investigated.

The goals of this study are to (1) identify likely semidiurnal internal tide generation sites and pathways, (2) specify the dissipation characteristic of the semidiurnal internal tides, and (3) study the interference of internal tides from two almost parallel ridges. The remainder of this paper is arranged as follows: Section 2 presents the numerical model and model setups, analysis methods, and model validation. Section 3 analyzes the spatial patterns of the semidiurnal barotropic-to-baroclinic energy conversion rate, energy fluxes, and dissipation. Semidiurnal standing waves are discussed in Section 4. Section 5 presents our conclusions.

2 Methods

2.1 *Numerical model and model setup*

The numerical modeling is conducted using the Massachusetts Institute of Technology general circulation model (MITgcm) (Marshall et al., 1997). The simulation has a horizontal resolution of about 1.7 km × 1.7 km [$\Delta x = (1/32)°, \Delta y = (1/64)°$]. In the vertical, there are 100 layers with thickness increasing from 5 m in the upper 200 m to 240 m near the bottom. The bottom stress is parameterized using a quadratic scheme with a bottom drag coefficient of 0.002 5. A sponge layer is imposed over 20 grid cells at each lateral boundary to suppress the reflection of baroclinic waves (Li, 2014; Zeng et al., 2021). We use hydrostatic approximation, which is suited for the simulation of internal tides with horizontal scales notably larger than vertical scales.

The initial and boundary conditions are extracted from Hybrid Coordinate Ocean Model (HYCOM) data (http://tds.hycom.org/thredds/catalog.html) (Chassignet et al., 2007). The model is initialized with spatially interpolated HYCOM time-averaged data from January to March 2020. It is forced with HYCOM time-averaged data from January to March 2020 for the subtidal circulation forcing at the open boundaries. Eight major tidal constituents (M_2, S_2, N_2, K_2, K_1, P_1, O_1, and Q_1) are applied as tidal forcing at the open boundaries. The amplitudes and phases of these tides are derived from the TOPEX/Poseidon Global Inverse Solution 7.2 (TPXO 7.2) (Egbert and Erofeeva, 2002).

The horizontal viscosity A_h and diffusivity λ_h are both set to 10^{-2} m^2/s. The vertical viscosity A_z and diffusivity λ_z are estimated according to the PP81 scheme (Pacanowski and Philander, 1981) as follows:

$$\begin{cases} A_z = \dfrac{\nu_0}{(1+\alpha\, Ri)^n} + \nu_b, \\ \lambda_z = \dfrac{A_z}{1+\alpha\, Ri} + \kappa_b, \end{cases} \tag{1}$$

where $\nu_b = 10^{-5}$ m^2/s and $\kappa_b = 10^{-5}$ m^2/s represent the background viscosity and diffusivity, respectively; $\nu_0 = 1.5 \times 10^{-2}$ m^2/s, $\alpha = 5$, and $n = 1$ are the adjustable parameters; $Ri = N^2(z)/(u_z^2 + v_z^2)$ is the Richardson number, u and v are zonal and meridional velocities; and $N(z)$ is the buoyancy frequency. These parameters have been verified in previous studies on internal tide dynamics (Vlasenko et al., 2018; Min et al., 2023).

We use the polynomial equation of state (EOS), known as the MDJWF equation (McDougall et al., 2003). The model bathymetry is based on the General Bathymetric Chart of the Oceans (GEBCO) dataset, which has a 15 arc-second resolution. The time step of the model is set to 10 s to satisfy the Courant–Friedrichs–Lewy (CFL) condition. The simulation is run for 30 d, and results from the final 15 d are used for detailed analyses. The model output is saved hourly. The simulated results are semidiurnal band-pass-filtered (10–16 h) to focus on the semidiurnal internal tides.

2.2 *Theory*

The depth-integrated, period-averaged baroclinic energy equation is (Buijsman et al., 2012a; Siyanbola et al., 2024)

$$\langle \overline{C} \rangle = \nabla \cdot \langle \overline{F} \rangle + \langle \overline{D} \rangle + R, \tag{2}$$

where C is the barotropic-to-baroclinic energy conversion rate, F denotes the baroclinic energy flux, D is the dissipation term due to eddy viscosity, and R is a residual term that includes the energy tendency term, wave-wave and wave-mean flow interaction terms, and offline computation errors. The brackets $\langle\ \rangle$ denote the integration from the bottom to the surface, and the overbar represents time averaging.

The perturbation density is

$$\rho'(x,y,z,t)=\rho(x,y,z,t)-\rho_{\mathrm{b}}(x,y,z)-\rho_0, \tag{3}$$

where ρ is the instantaneous density, ρ_{b} is the background density, and ρ_0 is the constant reference density. The horizontal perturbation velocity due to wave motion is

$$\boldsymbol{u}'(z,t)=\boldsymbol{u}(z,t)-\overline{\boldsymbol{u}}(z)-\boldsymbol{U}(t), \tag{4}$$

where $\boldsymbol{u}=(u,v)$ is the instantaneous velocity, $\overline{\boldsymbol{u}}$ is the time-mean of that velocity, and $\boldsymbol{U}$ is the horizontal barotropic velocity calculated according to the baroclinicity requirement as follows:

$$\frac{1}{H+\eta}\int_{-H}^{\eta}\boldsymbol{u}'(z,t)\,\mathrm{d}z=0. \tag{5}$$

where H is the depth and η is the sea surface elevation.

The perturbation pressure is

$$p'(z,t)=p_{\mathrm{surf}}(t)+\int_{z}^{\eta}\rho'(\hat{z},t)\,g\,\mathrm{d}\hat{z}, \tag{6}$$

$$p_{\mathrm{surf}}(t)=-\frac{1}{H+\eta}\int_{-H}^{\eta}\int_{z}^{\eta}\rho'(\hat{z},t)\,g\,\mathrm{d}\hat{z}\mathrm{d}z, \tag{7}$$

where g is the gravitational acceleration. The horizontal baroclinic energy flux is determined by

$$\boldsymbol{F}=\boldsymbol{u}'p'. \tag{8}$$

The depth-integrated barotropic-to-baroclinic energy conversion rate is defined as

$$\langle C\rangle=p'(-H,t)\,w_{\mathrm{bt}}, \tag{9}$$

where $w_{\mathrm{bt}}=\boldsymbol{U}\cdot\nabla\langle -H\rangle$ is the vertical component of barotropic velocity. The energy dissipation term D in Eq. (2) is calculated as (Buijsman et al., 2012a; Siyanbola et al., 2024)

$$D=\rho_0\varepsilon=\rho_0 A_{\mathrm{h}}\left[\left(\frac{\partial u'}{\partial x}\right)^2+\left(\frac{\partial u'}{\partial y}\right)^2+\left(\frac{\partial v'}{\partial x}\right)^2+\left(\frac{\partial v'}{\partial y}\right)^2\right]+\rho_0 A_{\mathrm{z}}\left[\left(\frac{\partial u'}{\partial z}\right)^2+\left(\frac{\partial v'}{\partial z}\right)^2\right], \tag{10}$$

where ε is the dissipation rate, and u' and v' are the baroclinic horizontal velocities along the x and y coordinates, respectively. Baroclinic horizontal kinetic energy (HKE) density is determined by

$$\mathrm{HKE}=\frac{1}{2}\rho_0\left(u'^2+v'^2\right). \tag{11}$$

Baroclinic available potential energy (APE) density is determined by

$$\mathrm{APE}=\int_{z-\zeta}^{z}g\left[\rho_{\mathrm{b}}(z)+\rho'(z)-\rho_{\mathrm{b}}(z')\right]\mathrm{d}z', \tag{12}$$

where ζ is the vertical displacement of a fluid particle due to wave motion.

The criticality parameter is calculated as

$$\gamma=|\nabla H|\Big/\sqrt{(\omega^2-f^2)/(N^2-\omega^2)}, \tag{13}$$

which is the ratio between the bottom topography slope and the internal tide beam angle, where $|\nabla H|=\sqrt{(\partial H/\partial x)^2+(\partial H/\partial y)^2}$. The criticality parameter is used to distinguish between supercritical topography ($\gamma>1$) and subcritical topography ($\gamma<1$). The topography is critical when $\gamma=1$ (Kang and Fringer, 2012).

2.3 *Model validation*

The simulated tidal velocity ellipses of the two major semidiurnal tidal constituents (M_2 and S_2) are consistent with the TPXO results (Fig. 2). The minor differences near the SSR are probably caused by differences in topography between our model and the TPXO solution. The magnitudes of the M_2 and S_2 constituents are very similar, with maximum velocity reaching about 0.1 m/s in the SSR region. The directions of the major axes of two constituents' tidal ellipses are generally consistent. The major axes are perpendicular to the isobaths in the SSR region, which favors the generation of internal waves.

The modeled sea surface heights are then compared with the tide gauge data provided by Howard et al. (2020) at the stations labeled in Fig. 1a. The absolute root-mean-square error (RMSE) is calculated following Cummins and Oey (1997) as

$$E=\sqrt{\frac{1}{2}\left(A_{\mathrm{o}}^2+A_{\mathrm{m}}^2\right)-A_{\mathrm{o}}A_{\mathrm{m}}\cos\left(G_{\mathrm{o}}-G_{\mathrm{m}}\right)}, \tag{14}$$

where A is the tidal amplitude, G is the phase, and subscripts o and m indicate observations and model, respectively. For the tide gauge near the SOP (Table 1), the estimated E for the M_2 and S_2 tidal constituents is 0.014 m and 0.035 m, respectively. The relative error E/A_{o}, is 3.1% and 13.8%, respectively (mean error 8.5%). For the tide gauge near the Antarctic Peninsula (Fig. 1a), the relative error is 8.3% and 15.0%, respectively (mean error 11.7%). These data indicate that the model results are generally

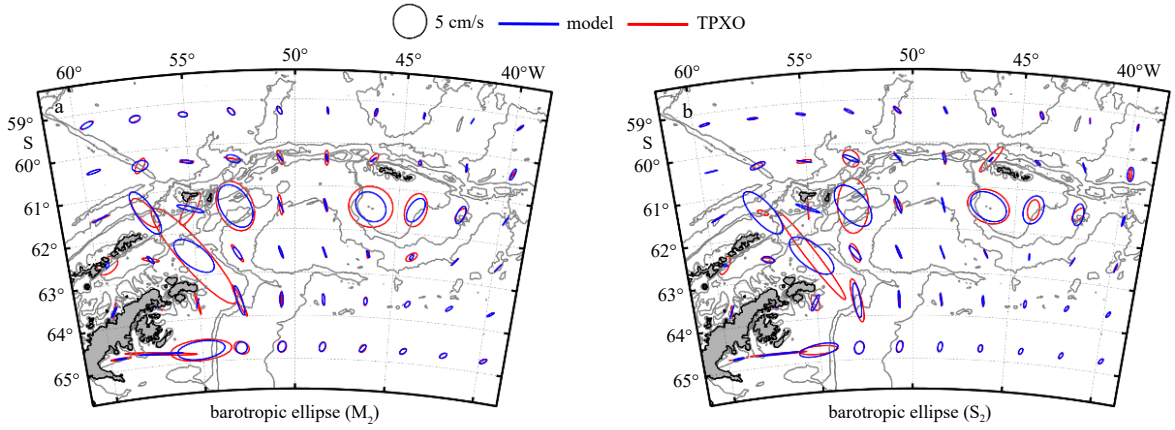


Fig. 2. Comparison between modeled and TPXO M_2 (a) and S_2 (b) tidal velocity ellipses. Blue tidal ellipses are the barotropic M_2 and S_2 constituents from the model, and red ellipses are TPXO predictions for the M_2 and S_2 constituents. Bathymetry contours are −100 m, −500 m, −1 000 m, −3 000 m, and −5 000 m.

Table 1. Comparisons of observed (Obs) and modeled (Mod) tidal components (M_2, S_2) amplitudes and phases at the three stations shown in Fig. 1a

Station	Constituent	Amplitude(Obs/Mod)/cm	Phase(Obs/Mod)/(°)	E/cm	(E/A_o)/%
S1 (45.6°W, 60.7°S)	M_2	45.3/44.2	264.1/266.3	1.4	3.1
S1 (45.6°W, 60.7°S)	S_2	25.2/28.8	290.7/297.8	3.5	13.8
S2 (54.717°W, 60.85°S)	M_2	43.4/42.0	277.0/279.9	1.8	4.2
S2 (54.717°W, 60.85°S)	S_2	21.7/26.7	323.0/328.1	3.9	18.0
S3 (56.983°W, 63.383°S)	M_2	63.0/57.2	275.0/279.4	5.2	8.3
S3 (56.983°W, 63.383°S)	S_2	40.0/45.3	312.0/320.8	6.0	15.0

Note: E and A_o are defined in Eq. (14).

consistent with the tide gauge data. The above analysis confirms the reliability of semidiurnal barotropic tide simulation.

3 Results

3.1 *Sources and energetics of the semidiurnal internal tides*

In what follows we evaluate the depth-integrated, tidally averaged values of Eq. (2). Time averaging is performed over the last 15 d of the simulation. The depth-integrated, tidally averaged barotropic to baroclinic semidiurnal conversion rates are shown in Fig. 3. The spatial distribution of the conversion rates suggests multiple sources of semidiurnal internal tides in the Weddell-Scotia Confluence. The conversion rates are significant mainly along the SSR. The barotropic to baroclinic energy conversion rate over the SSR reaches 0.3 W/m^2, which is comparable with that of some semidiurnal internal tide hotspots in the Pacific Ocean (e.g., I-Lan Ridge, Southern California Bight, and Aleutian Archipelago, the Izu-Ogasawara Ridge) (Buijsman et al., 2012b; Masunaga et al., 2018; Chang et al., 2019; You et al., 2023).

The three primary semidiurnal internal tides sources are indicated by three boxes in Fig. 3a. In the SFZ region (Box Ⅰ) the area-integrated conversion rate is 0.13 GW. Morozov (2018) used mooring observations and numerical modeling to show that internal tides can be generated from Shackleton Ridge. The area-integrated conversion rate in Box Ⅱ is 0.71 GW, much larger than that of Box Ⅰ and Box Ⅲ (0.07 GW). As shown in Figs 3b and c, the barotropic to baroclinic energy conversion occurs mainly in areas with critical and supercritical topography. Some negative conversion occurs in the SSR region, due to the interference of multiple semidiurnal internal tide sources (Zilberman et al., 2009; Kelly and Nash, 2010; Kang and Fringer, 2012). Since the main barotropic to baroclinic semidiurnal energy conversion occurs in the area indicated by Box Ⅱ (contributes about 70% of the total conversion), the following sections will focus on this region.

3.2 *Radiation paths of the semidiurnal internal tides*

Spatial maps of depth-integrated, tidally averaged baroclinic energy fluxes illustrate the radiation paths of the semidiurnal internal tides (Fig. 4). The semidiurnal internal tides energy fluxes are largest near the SSR (with a magnitude of about 2 kW/m). The semidiurnal internal tides generated over the SSR and PR propagate northward to the Scotia Sea and southward to the Powell Basin.

The energy fluxes show south-north asymmetry in the SSR region. The northward energy fluxes spread, and the southward energy fluxes tended to focus due to the arc-

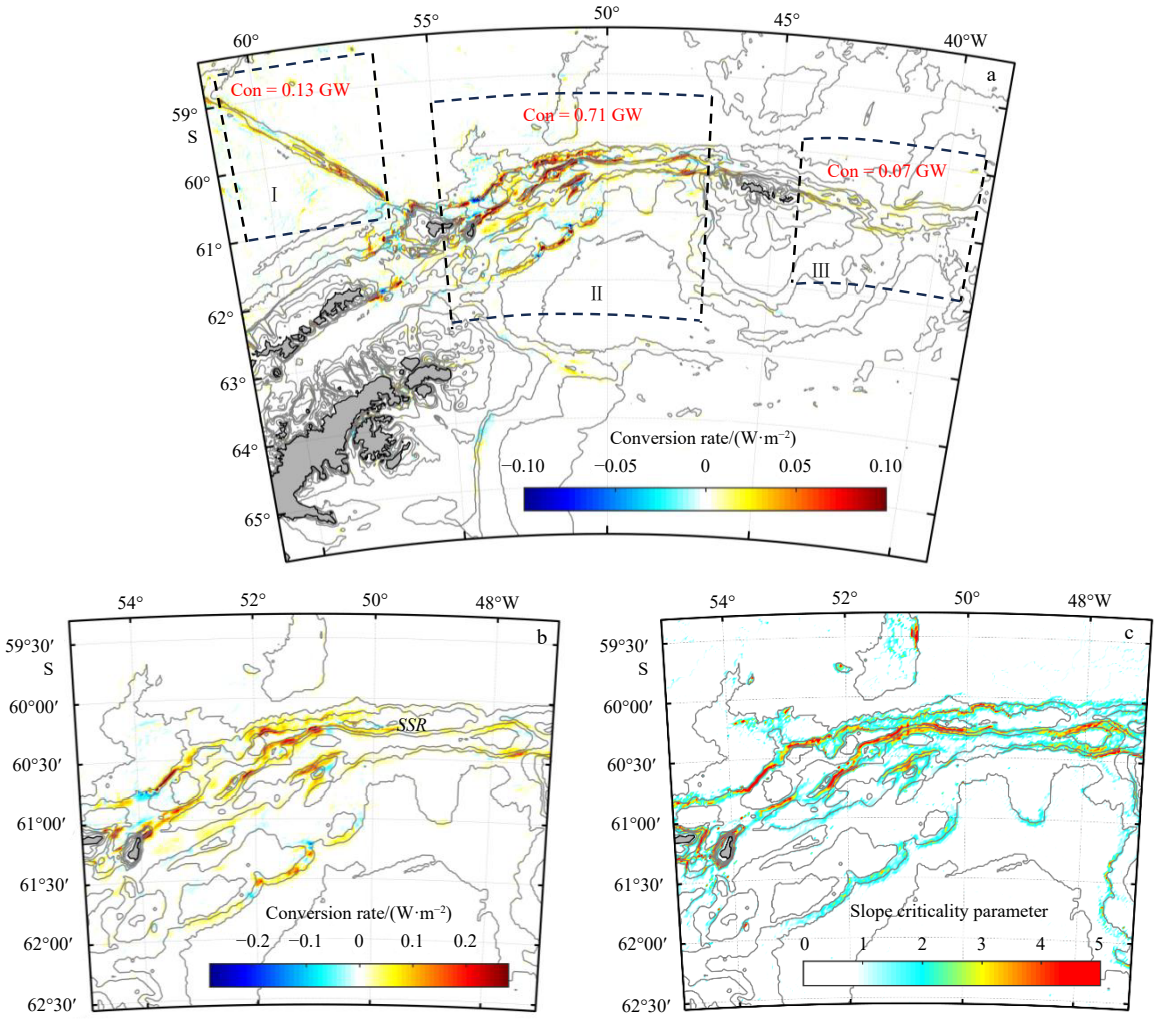


Fig. 3. Depth-integrated, tidally averaged barotropic to baroclinic semidiurnal energy conversion rates (a), an enlargement of Box Ⅱ shown in a (b), and the slope criticality parameter $\gamma = |\nabla H| \Big/ \sqrt{(\omega^2 - f^2)/(N^2 - \omega^2)}$ for the semidiurnal M_2 frequency in the region shown in b (c). Bathymetry contours are −100 m, −200 m, −300 m, −500 m, −800 m, −2 000 m, −3 000 m, and −5 000 m. Con represents the area-integrated conversion rate. SSR: South Scotia Ridge.

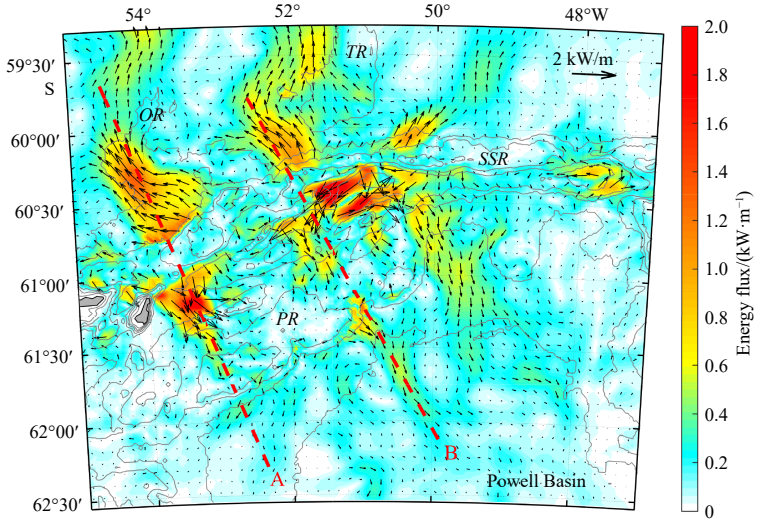


Fig. 4. Depth-integrated, tidally averaged semidiurnal energy fluxes (Region Ⅱ in Fig. 3a). The background color shows the magnitude of the semidiurnal energy fluxes. The red dashed lines represent Transects A and B that shown in Figs 5 and 7. TR: Terror Rise; OR: Ona Rise; PR: Philip Ridge; SSR: South Scotia Ridge.

like SSR. The northward energy fluxes entering the Scotia Sea are stronger than the southward energy fluxes entering the Powell Basin. The energy flux pathways are significantly modified by the small topography features. For example, the northward propagating energy fluxes, indicated by Transect B, meander due to the Terror Rise. The northward energy fluxes indicated by Transect A are modified by the Ona Rise (Fig. 4). East of Transect B, semidiurnal internal tides with energy fluxes of about 0.6 kW/m propagate southward to the Powell Basin and almost all the way along the isobath.

Anticlockwise energy flux patterns form over the region between SSR and PR. The anticlockwise energy flux patterns are generated by internal tide interference from two sources, which will be discussed below. Away from the SSR and PR, the semidiurnal internal tide's southward and northward energy fluxes decrease gradually due to dissipation. The energy flux of the semidiurnal internal tides in the Powell Basin is only about 0.2 kW/m, 10% of the maximum energy flux over the SSR.

To visualize the vertical structure of the propagating internal tides, we plot snapshots of meridional baroclinic velocity (at t = 28.625 d) along Transects A and B (indicated in Fig. 4), as shown in Fig. 5. The baroclinic velocity reaches about 0.3 m/s over the SSR and PR (Fig. 5). The baroclinic velocities form an internal beam near the source region, reflecting between the sea surface and sea bottom (Fig. 5).

The internal tide beam, formed by the superposition of multiple internal wave modes, suggests that high-mode internal waves exist in the SSR region. The internal tide beams emanate from the two ridges, which agrees with the generation sites shown in Fig. 3. The model-predicted internal tide beams are consistent with the theoretical vertical internal tidal beams (dashed lines in Fig. 5) calculated as

$$\frac{\mathrm{d}z}{\mathrm{d}x} = \pm\left(\frac{\omega^2 - f^2}{N^2 - \omega^2}\right)^{-0.5}, \tag{15}$$

where ω, N, and f are the tidal, buoyancy, and inertial frequencies, respectively.

3.3 *Energy dissipation*

The depth-integrated, tidally averaged energy dissipation of semidiurnal internal tides estimated by Eq. (10) is shown in Fig. 6a. The two ridges (SSR and PR) feature high levels of baroclinic energy dissipation. The areas with high-level dissipation coincide with the semidiurnal internal tide sources, as shown in Fig. 3. Areas in the SSR region with high barotropic-to-baroclinic conversion feature high energy dissipation. The energy dissipation of the semidiurnal internal tides in the SSR can reach up to 10^{-1} W/m^2, comparable to other semidiurnal internal tide hotspots [e.g., Aleutian Ridge in the Pacific (You et al., 2023] and Monterey Bay (Kang and Fringer, 2012). The area-integrated dissipation rate is 0.56 GW, 79% of the area-integrated barotropic-to-baroclinic conversion. The high fraction of the barotropic-to-baroclinic conversion lost to local dissipation in the SSR region is also found in

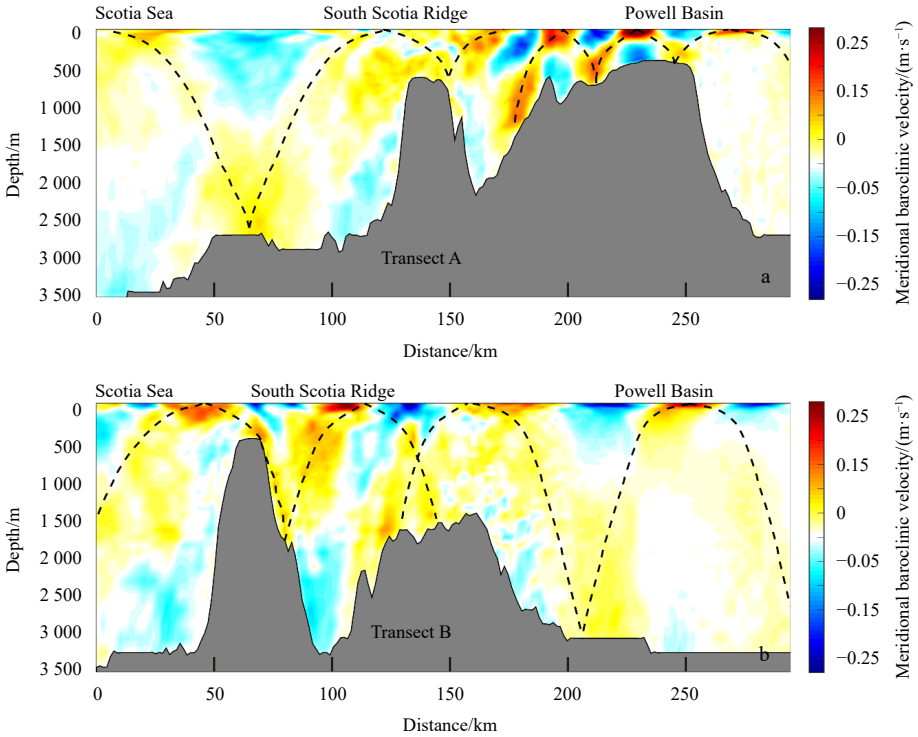


Fig. 5. A snapshot of the modeled vertical section of meridional baroclinic velocity along Transect A (a) and Transect B (b) shown in Fig. 4 at t = 28.625 d. The dashed lines indicate theoretical vertical internal tidal beams.

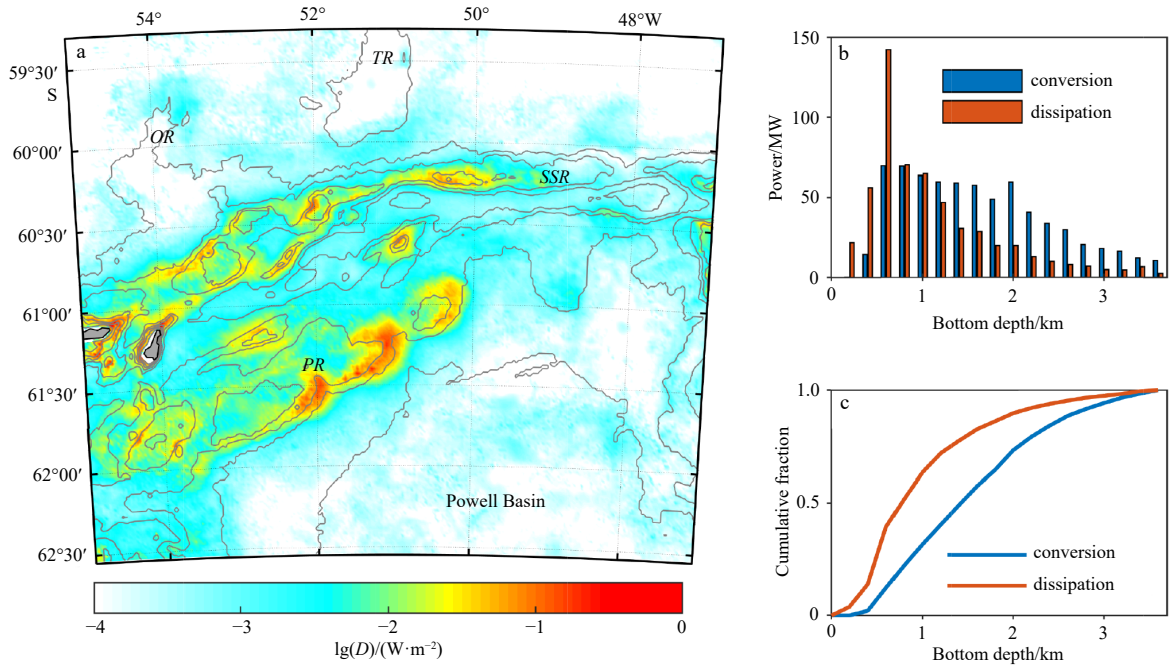


Fig. 6. Spatial distribution of the depth-integrated, tidally averaged energy dissipation of the semidiurnal internal tides over the SSR (Region Ⅱ in Fig. 3a) (a), distribution of energy conversion and dissipation as a function of bottom depth (b), and cumulative fraction of b (c). Bathymetry contours are spaced at −100 m, −200 m, −300 m, −500 m, −800 m, −2 000 m, −3 000 m, and −5 000 m. TR: Terror Rise; OR: Ona Rise; PR: Philip Ridge; SSR: South Scotia Ridge.

other semidiurnal internal tide hotspots. Nagai and Hibiya (2015) reported that 50%–100% of internal tide energy was dissipated near their generation sites in the Indonesian seas. You et al. (2023) revealed that semidiurnal internal tides dissipated 50%–72% of their energy in the Aleutian Archipelago.

Far from the SSR, the semidiurnal internal tide's energy dissipation decreases. When the semidiurnal internal tides propagate to the Powell Basin, the dissipation rate decreases to 10^{-3}–10^{-4} W/m^2. In the Scotia Sea, the dissipation decreases to approximately 10^{-4} W/m^2. The area-integrated energy conversion and dissipation terms in 200-m depth bins and the cumulative fractions are shown in Figs 6b and c for the area shown in Fig. 6a. The energy dissipation of semidiurnal internal tides occurs mainly in the shallow regions. Approximately 60% of the total dissipation occurs in depths shallower than 1 000 m. The dissipation of the semidiurnal internal tides is stronger than the conversion in regions shallower than 1 000 m (Figs 6b and c), suggesting the dissipation of remote internal tides generated in the region deeper than 1 000 m.

The vertical structures of the dissipation rates along Transects A and B are shown in Fig. 7. As Fig. 7 indicates, the dissipation rates are nonuniform. High tidal dissipation rates occur mainly in the upper 100 m near the crest of the SSR and PR, due to strong velocity shear induced by the semidiurnal internal tide. The dissipation rate reaches 10^{-7} W/kg over the SSR and PR crest, with high dissipation above the bottom topography. For the upper 100 m, at which the pycnocline lies, the dissipation rate is approximately 10^{-9} W/kg. The magnitude of the dissipation is similar to that obtained through field observation in the SSR region by Lin et al. (2022) and Guo et al. (2016). This result indicates that internal tide dissipation near the surface can be a source of enhanced mixing.

As shown in Fig. 5, the internal tide beam impacts the other ridge after one reflection from the sea surface. According to Buijsman et al. (2012a), this should create a constructive interference pattern over the SSR region. The constructive interference between the internal tides generated from the two crests will enhance the conversion and dissipation over the SSR. As Fig. 7 shows, the two ridges and Hesperides Trough have a high dissipation rate. The dissipation distribution is similar to that in the Luzon Strait, which also has double ridges, although has a lower dissipation level (Buijsman et al., 2012a).

4 Discussion

Previous studies have shown that the superposition of two equal (unequal) amplitude progressive internal tides propagating in opposite directions could lead to the formation of a purely (partly) standing wave (Martini et al., 2007; Aslam et al., 2018). In partly standing waves, the ratio of HKE over APE will oscillate sinusoidally, deviating from the theoretical value (Hall et al., 2014; Johnston et al., 2015).

As shown in Fig. 4, an anticlockwise semidiurnal energy flux gyre formed between the SSR and PR, indicating a partly standing wave. Similar phenomena have been found in Luzon Strait and the Bay of Bengal (Buijsman et al., 2014; Jithin et al., 2019). Min et al. (2023) found

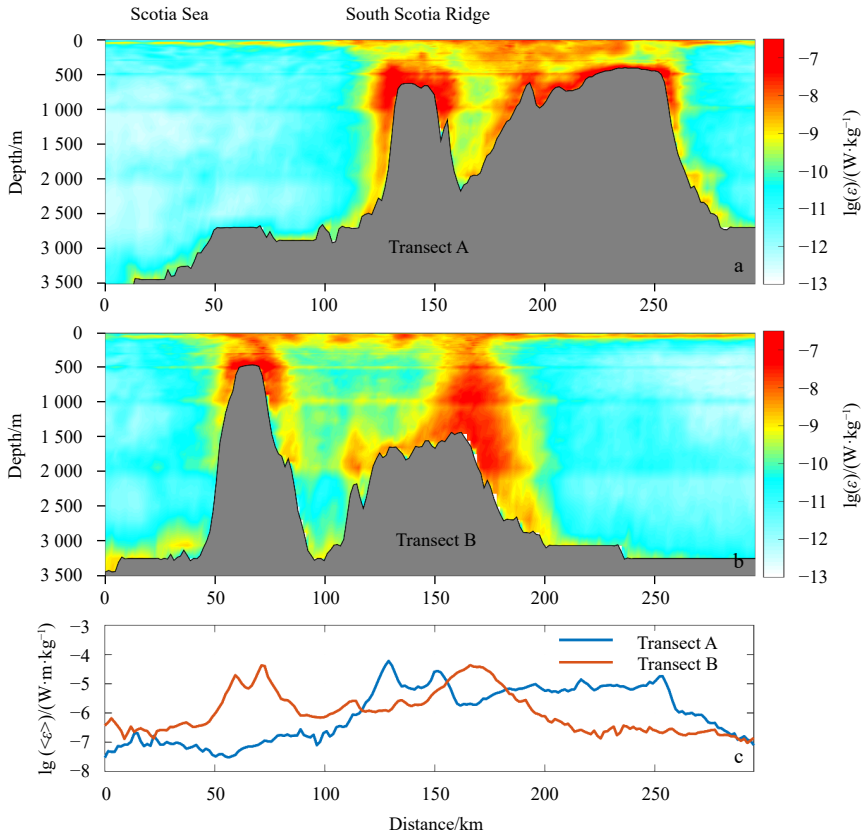


Fig. 7. Cross-section of the tidally averaged dissipation rate along Transect A (a) and Transect B (b) shown in Fig. 4 and the depth-integrated of a and b (c).

partly standing waves over a double-canyon region in the southern East China Sea. To study the characteristics of the standing waves more closely, we calculate the HKE and APE of the semidiurnal internal tides. Figure 8 shows the spatial distribution of the depth-integrated, tidally averaged HKE and APE overlaid with energy fluxes. High HKE appears over the Hesperides Trough while high APE appears at the two ridges. High HKE appears at the center of the anticlockwise energy flux gyre, and high APE appears at one-quarter wavelength away.

For a progressive internal wave, the ratio of HKE over APE is calculated as

$$\frac{\mathrm{HKE}}{\mathrm{APE}} = \frac{\omega^2 + f^2}{\omega^2 - f^2}. \tag{16}$$

For semidiurnal M_2 internal tides at latitude 60.5°S, the theoretical ratio of HKE over APE is 9.6. Since the SSR lies in a high latitude area, the theoretical ratio of HKE over APE is larger than it would be for a low latitude area.

Figure 9 shows the HKE and APE vertical structures

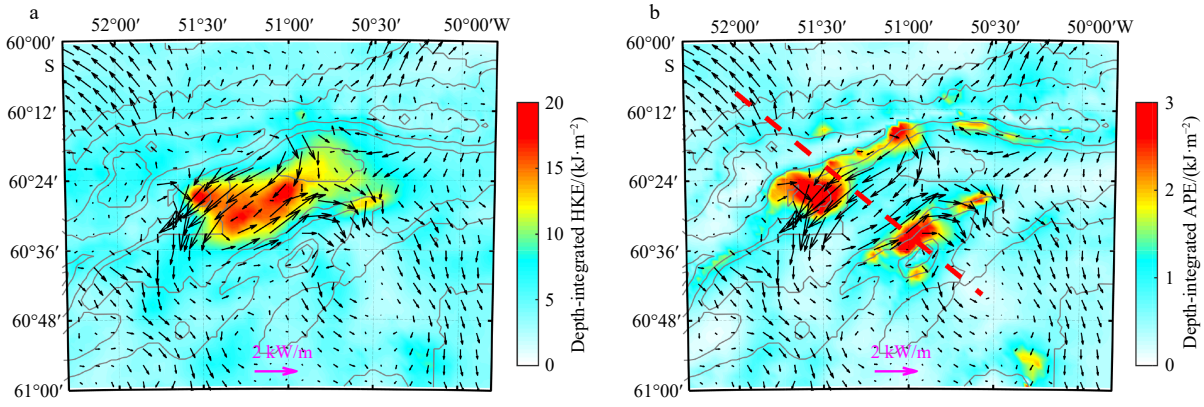


Fig. 8. Spatial distribution of depth-integrated, tidally averaged HKE (a) and APE (b) of the semidiurnal internal tides with the depth-integrated, tidally averaged energy fluxes arrows. The red dashed line in b is the transect shown in Fig. 9. HKE: horizontal kinetic energy; APE: available potential energy.

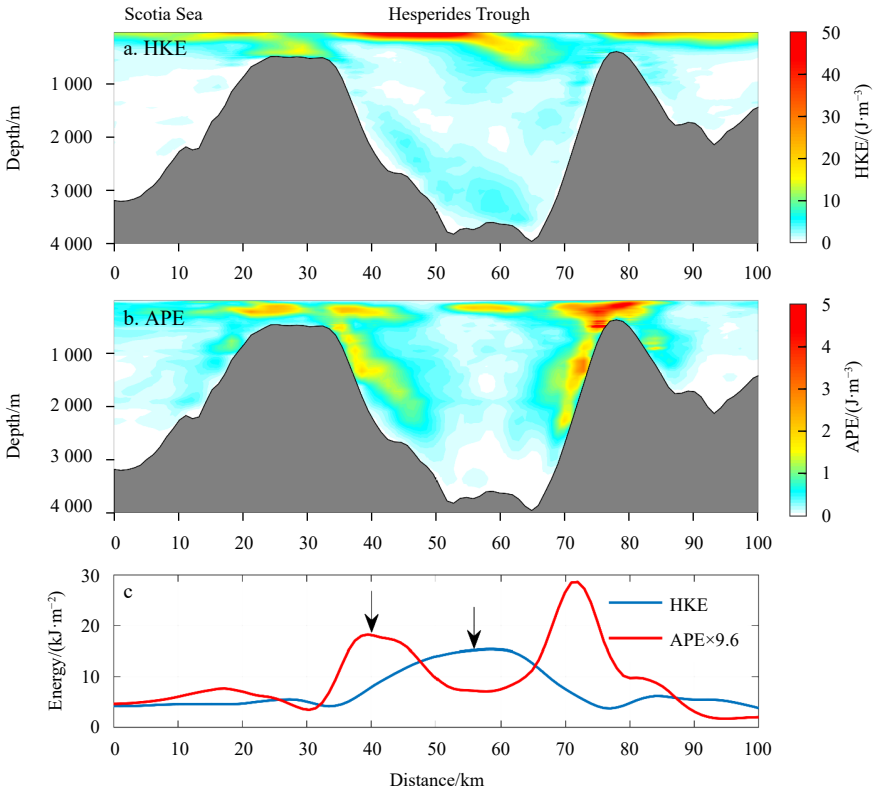


Fig. 9. Cross-section of the tidally averaged semidiurnal HKE (a) and APE (b) along the transect shown in Fig. 8b, and HKE and APE (c). In c, the APE has been exaggerated by 9.6 to facilitate comparison. The arrow in c show the peaks of HKE and APE. HKE: horizontal kinetic energy; APE: available potential energy.

along the transect indicated in Fig. 8b. High HKE occurs at the upper 200 m at the Hesperides Trough while high APE occurs over the two ridge slopes (Figs 9a and b). The depth-integrated, tidally averaged HKE and APE along the transect oscillate sinusoidally between the two ridges. As the two arrows in Fig. 9c show, the distance between the HKE and APE peaks is about 16 km, about one-quarter of the mode-1 internal tide wavelength (70 km). This energy pattern indicates the formation of partly standing waves between the two ridges. Away from the Hesperides Trough, the ratio of the HKE over APE approximates the theoretical values of a progressive internal wave (Fig. 9c). Partly standing waves also exist on the west and east sides of the Hesperides Trough (results not shown).

According to previous studies, the interference of internal tides from the SSR and PR will enhance conversion and dissipation. However, the detailed mechanisms for this process in this region have not been addressed. The detailed interference process and the role of each crest need to be further investigated. Furthermore, we consider only the semidiurnal internal tide generated in austral summer. Stratification is a crucial factor influencing the generation and evolution of internal tides (Li et al., 2023). Thus, the stratification in austral winter needs to be incorporated into the model. Finally, the formation and existence of sea ice in the winter can change stratification and ocean surface stress, significantly affecting the internal tide generation and dissipation processes. Therefore, a fully coupled ice-ocean simulation should be attempted.

5 Conclusions

We investigate the generation, propagation, and dissipation of semidiurnal internal tides in the Weddell-Scotia Confluence using a high-resolution numerical simulation. The numerical model predicts the barotropic tides reasonably well, and the predicted semidiurnal tides are consistent with TPXO results and tide gauge data.

We conclude that semidiurnal internal tides are generated due to the relatively strong tidal currents and steep bottom topography in the Weddell-Scotia Confluence. The model results show that the SSR and PR between the AP and the SOP are generation sites of semidiurnal internal tides. The depth-integrated, tidally averaged barotropic to baroclinic conversion rate reaches as high as 0.3 W/m^2. The area-integrated semidiurnal conversion rate is 0.71 GW. The depth-integrated, tidally averaged energy fluxes of the semidiurnal internal tide reach 2 kW/m over the SSR. The adjacent Shackleton Fracture Zone region is also a generation site of internal tides with low barotropic to baroclinic energy conversion.

Internal tide beams are visible near the ridges, indicating high-mode internal waves are generated during the tide-topography interactions. The modeled internal tide beams correlate well with the theoretical internal tide beams. As the semidiurnal internal tides propagate away

from the sources, the energy decreases gradually due to dissipation. The strong dissipation of semidiurnal internal tides occurs over the SSR and PR. The energy dissipation over the SSR reaches up to 10^{-1} W/m^2. Away from the ridge, the dissipation decreases to 10^{-5} W/m^2. The crests of the ridges are hotspots of high energy dissipation up to 10^{-7} W/kg. The area-integrated dissipation rate is 0.56 GW, 79% of the barotropic-to-baroclinic conversion.

The semidiurnal internal tides generated from the two parallel crests of the SSR and PR interfere, forming a partly standing wave between the two ridges. The energy fluxes of semidiurnal internal tides create an anticlockwise gyre between the two ridges. The HKE and APE oscillate sinusoidally with peaks at quarter-wavelength intervals. The semidiurnal internal tides and related dissipation affect the circulation and mass transport in the Weddell-Scotia Confluence and need to be considered in the analysis of overturning circulation.

References

Alford M H, Peacock T, MacKinnon J A, et al. 2015. The formation and fate of internal waves in the South China Sea. Nature, 521(7550): 65–69, doi: 10.1038/nature14399

Aslam T, Hall R A, Dye S R. 2018. Internal tides in a dendritic submarine canyon. Progress in Oceanography, 169: 20–32, doi: 10.1016/j.pocean.2017.10.005

Bennetts L G, Shakespeare C J, Vreugdenhil C A, et al. 2024. Closing the loops on southern ocean dynamics: From the circumpolar current to ice shelves and from bottom mixing to surface waves. Reviews of Geophysics, 62(3): e2022RG000781, doi: 10.1029/2022RG000781

Buijsman M C, Klymak J , Legg S, et al. 2014. Three-dimensional double-ridge internal tide resonance in Luzon Strait. Journal of Physical Oceanography, 44(3): 850–869, doi: 10.1175/jpo-d-13-024.1

Buijsman M C, Legg S, Klymak J. 2012a. Double-ridge internal tide interference and its effect on dissipation in Luzon Strait. Journal of Physical Oceanography, 42(8): 1337–1356, doi: 10.1175/JPO-D-11-0210.1

Buijsman M C, Stephenson G R, Ansong J K, et al. 2020. On the interplay between horizontal resolution and wave drag and their effect on tidal baroclinic mode waves in realistic global ocean simulations. Ocean Modelling, 152: 101656, doi: 10.1016/j.ocemod.2020.101656

Buijsman M C, Uchiyama Y, McWilliams J C, et al. 2012b. Modeling semidiurnal internal tide variability in the Southern California Bight. Journal of Physical Oceanography, 42(1): 62–77, doi: 10.1175/2011JPO4597.1

Chang Hang, Xu Zhenhua, Yin Baoshu, et al. 2019. Generation and propagation of M_2 internal tides modulated by the Kuroshio Northeast of Taiwan. Journal of Geophysical Research: Oceans, 124(4): 2728–2749, doi: 10.1029/2018JC014228

Chassignet E P, Hurlburt H E, Smedstad O M, et al. 2007. The HYCOM (HYbrid Coordinate Ocean Model) data assimilative system. Journal of Marine Systems, 65(1): 60–83, doi: 10.1016/j.jmarsys.2005.09.016

Cummins P F, Oey L Y. 1997. Simulation of barotropic and baroclinic tides off Northern British Columbia. Journal of Physical Oceanography, 27(5): 762–781, doi: 10.1175/1520-0485(1997)027<0762:SOBABT>2.0.CO;2

Egbert G D, Erofeeva S Y. 2002. Efficient inverse modeling of barotropic ocean tides. Journal of Atmospheric and Oceanic Technology, 19(2): 183–204, doi: 10.1175/1520-0426(2002)019<0183:Eimobo>2.0.Co;2

Guo Guijun, Shi Jiuxin, Jiao Yutian. 2016. Turbulent mixing in the upper ocean of the northwestern Weddell Sea, Antarctica. Acta Oceanologica Sinica, 35(3): 1–9, doi: 10.1007/s13131-016-0816-y

Hall R A, Alford M H, Carter G S, et al. 2014. Transition from partly standing to progressive internal tides in Monterey Submarine Canyon. Deep-Sea Research Part Ⅱ: Topical Studies in Oceanography, 104: 164–173, doi: 10.1016/j.dsr2.2013.05.039

Hamann M M, Alford M H, Lucas A J, et al. 2021. Turbulence driven by reflected internal tides in a supercritical submarine canyon. Journal of Physical Oceanography, 51(2): 591–609, doi: 10.1175/JPO-D-20-0123.1

Heywood K J, Collins J L, Hughes C W, et al. 2007. On the detectability of internal tides in Drake Passage. Deep-Sea Research Part Ⅰ: Oceanographic Research Papers, 54(11): 1972–1984, doi: 10.1016/j.dsr.2007.08.002

Howard S L, King M, Padman L. 2020. Antarctic Tide Gauge Database, version 1. U. S. Antarctic Program (USAP) Data Center. https://www.usap-dc.org/view/dataset/601358 [2024-08-01]

Jithin A K, Francis P A, Unnikrishnan A S, et al. 2019. Modeling of internal tides in the western bay of Bengal: Characteristics and energetics. Journal of Geophysical Research: Oceans, 124(12): 8720–8746, doi: 10.1029/2019jc015319

Johnston T M S, Rudnick D L, Kelly S M. 2015. Standing internal tides in the Tasman Sea observed by gliders. Journal of Physical Oceanography, 45(11): 2715–2737, doi: 10.1175/JPO-D-15-0038.1

Kang Dujuan, Fringer O. 2012. Energetics of barotropic and baroclinic tides in the Monterey Bay Area. Journal of Physical Oceanography, 42(2): 272–290, doi: 10.1175/jpo-d-11-039.1

Kelly S M, Nash J D. 2010. Internal-tide generation and destruction by shoaling internal tides. Geophysical Research Letters, 37(23): L23611, doi: 10.1029/2010GL045598

Kerry C G, Powell B S, Carter G S. 2013. Effects of remote generation sites on model estimates of M_2 internal tides in the Philippine Sea. Journal of Physical Oceanography, 43(1): 187–204, doi: 10.1175/jpo-d-12-081.1

Klymak J M, Pinkel R, Rainville L. 2008. Direct breaking of the internal tide near topography: Kaena Ridge, Hawaii. Journal of Physical Oceanography, 38(2): 380–399, doi: 10.1175/2007JPO3728.1

Li Qiang. 2014. Numerical assessment of factors affecting nonlinear internal waves in the South China Sea. Progress in Oceanography, 121: 24–43, doi: 10.1016/j.pocean.2013.

03.006

Li Qun, Wang Shuya, Chen Xu. 2023. Radiation and energetics of M_2 internal tides in the Okhotsk Sea. Deep-Sea Research Part Ⅰ: Oceanographic Research Papers, 199: 104131, doi: 10.1016/j.dsr.2023.104131

Lin Lijin, Shi Jiuxin, Yao Chenyang, et al. 2022. Turbulent mixing and its relationship with water mass and circulation in the upper ocean of the Weddell-Scotia Confluence, Antarctica. Chinese Journal of Polar Research (in Chinese), 34(1): 34–50, doi: 10.13679/j.jdyj.20210020

MacKinnon J A, Zhao Zhongxiang, Whalen C B, et al. 2017. Climate process team on internal wave-driven ocean mixing. Bulletin of the American Meteorological Society, 98(11): 2429–2454, doi: 10.1175/BAMS-D-16-0030.1

Marshall J, Adcroft A, Hill C, et al. 1997. A finite-volume, incompressible Navier Stokes model for studies of the ocean on parallel computers. Journal of Geophysical Research: Oceans, 102(C3): 5753–5766, doi: 10.1029/96JC02775

Martini K I, Alford M H, Nash J D, et al. 2007. Diagnosing a partly standing internal wave in Mamala Bay, Oahu. Geophysical Research Letters, 34(17): L17604, doi: 10.1029/2007GL029749

Masunaga E, Uchiyama Y, Suzue Y, et al. 2018. Dynamics of internal tides over a shallow ridge investigated with a high-resolution downscaling regional ocean model. Geophysical Research Letters, 45(8): 3550–3558, doi: 10.1002/2017GL076916

McDougall T J, Jackett D R, Wright D G, et al. 2003. Accurate and computationally efficient algorithms for potential temperature and density of seawater. Journal of Atmospheric and Oceanic Technology, 20(5): 730–741, doi: 10.1175/1520-0426(2003)20<730:Aaceaf>2.0.Co;2

Meredith M P, Meijers A S, Naveira Garabato A C, et al. 2015. Circulation, retention, and mixing of waters within the Weddell-Scotia Confluence, Southern Ocean: The role of stratified Taylor columns. Journal of Geophysical Research: Oceans, 120(1): 547–562, doi: 10.1002/2014JC010462

Min Wenjia, Li Qun, Xu Zhenhua, et al. 2023. High-resolution, non-hydrostatic simulation of internal tides and solitary waves in the southern East China Sea. Ocean Modelling, 181: 102141, doi: 10.1016/j.ocemod.2022.102141

Morozov E G. 2018. Internal tide in the Drake passage. Izvestiya, Atmospheric and Oceanic Physics, 54(6): 608–615, doi: 10.1134/S0001433818060117

Nagai T, Hibiya T. 2015. Internal tides and associated vertical mixing in the Indonesian Archipelago. Journal of Geophysical Research: Oceans, 120(5): 3373–3390, doi: 10.1002/2014JC010592

Nash J D, Kelly S M, Shroyer E L, et al. 2012. The unpredictable nature of internal tides on continental shelves. Journal of Physical Oceanography, 42(11): 1981–2000, doi: 10.1175/jpo-d-12-028.1

Naveira Garabato A C, McDonagh E L, Stevens D P, et al. 2002. On the export of Antarctic Bottom Water from the Weddell Sea. Deep-Sea Research Part Ⅱ: Topical Studies in Oceanography, 49(21): 4715–4742, doi: 10.1016/S0967-0645(02)00156-X

Pacanowski R C, Philander S G H. 1981. Parameterization of vertical mixing in numerical models of tropical oceans. Journal of Physical Oceanography, 11(11): 1443–1451, doi:10.1175/1520-0485(1981)011<1443:Povmin>2.0.Co;2

Padman L, Howard S, Muench R. 2006. Internal tide generation along the South Scotia Ridge. Deep-Sea Research Part Ⅱ: Topical Studies in Oceanography, 53(1−2): 157–171, doi: 10.1016/j.dsr2.2005.07.011

Padman L, Siegfried M R, Fricker H A. 2018. Ocean tide influences on the Antarctic and Greenland Ice Sheets. Reviews of Geophysics, 56(1): 142–184, doi: 10.1002/2016RG000546

Rainville L, Johnston T M S, Carter G S, et al. 2010. Interference pattern and propagation of the M_2 internal tide south of the Hawaiian Ridge. Journal of Physical Oceanography, 40(2): 311–325, doi: 10.1175/2009JPO4256.1

Robertson R. 2005. Baroclinic and barotropic tides in the Weddell Sea. Antarctic Science, 17(3): 461–474, doi: 10.1017/S0954102005002890

Robertson R, Padman L, Egbert G D. 1985. Tides in the Weddell Sea. In: Jacobs S S, Weiss R F, eds. Ocean, Ice, and Atmosphere: Interactions at the Antarctic Continental Margin. American Geophysical Union, 75: 341–369, doi: 10.1029/AR075p0341

Simmons H L, Hallberg R W, Arbic B K. 2004. Internal wave generation in a global baroclinic tide model. Deep-Sea Research Part Ⅱ: Topical Studies in Oceanography, 51(25−26): 3043–3068, doi: 10.1016/j.dsr2.2004.09.015

Siyanbola O Q, Buijsman M C, Delpech A, et al. 2024. Interactions of remotely generated internal tides with the U. S. west coast continental margin. Journal of Geophysical Research: Oceans, 129(6): e2023JC020859, doi: 10.1029/2023JC020859

St Laurent L C, Nash J D. 2004. An examination of the radiative and dissipative properties of deep ocean internal tides. Deep-Sea Research Part Ⅱ: Topical Studies in Oceanography, 51(25−26): 3029–3042, doi: 10.1016/j.dsr2.2004.09.008

Vlasenko V, Stashchuk N, Inall M E, et al. 2014. Tidal energy conversion in a global hot spot: On the 3-D dynamics of baroclinic tides at the Celtic Sea shelf break. Journal of Geophysical Research: Oceans, 119(6): 3249–3265, doi: 10.1002/2013JC009708

Vlasenko V, Stashchuk N, Nimmo-Smith W A M. 2018. Three-dimensional dynamics of baroclinic tides over a seamount. Journal of Geophysical Research: Oceans, 123(2): 1263–1285, doi: 10.1002/2017JC013287

Wang Xiaowei, Peng Shiqiu, Liu Zhiyu, et al. 2016. Tidal mixing in the South China Sea: An estimate based on the internal tide energetics. Journal of Physical Oceanography, 46(1): 107–124, doi: 10.1175/jpo-d-15-0082.1

Wang Yang, Xu Zhenhua, Hibiya T, et al. 2021. Radiation path of diurnal internal tides in the Northwestern Pacific controlled by refraction and interference. Journal of Geophys-

ical Research: Oceans, 126(11): e2020JC016972, doi: 10.1029/2020JC016972

Wang Yang, Xu Zhenhua, Yin Baoshu, et al. 2018. Long-range radiation and interference pattern of multisource M_2 internal tides in the Philippine Sea. Journal of Geophysical Research: Oceans, 123(8): 5091–5112, doi: 10.1029/2018jc013910

Waterhouse A F, MacKinnon J A, Nash J D, et al. 2014. Global patterns of diapycnal mixing from measurements of the turbulent dissipation rate. Journal of Physical Oceanography, 44(7): 1854–1872, doi: 10.1175/jpo-d-13-0104.1

You Jia, Xu Zhenhua, Li Qun, et al. 2023. M_2 internal tide energetics and behaviors in the subpolar North Pacific. Journal of Physical Oceanography, 53(5): 1269–1290, doi: 10.1175/JPO-D-22-0032.1

Zaron E D. 2019. Baroclinic tidal sea level from exact-repeat mission altimetry. Journal of Physical Oceanography, 49(1): 193–210, doi: 10.1175/jpo-d-18-0127.1

Zeng Zhi, Brandt P, Lamb K G, et al. 2021. Three-dimensional numerical simulations of internal tides in the angolan upwelling region. Journal of Geophysical Research: Oceans, 126(2): e2020JC016460, doi: 10.1029/2020JC016460

Zhao Zhongxiang, Alford M H, Girton J B, et al. 2016. Global observations of open-ocean mode-1 M_2 internal tides. Journal of Physical Oceanography, 46(6): 1657–1684, doi: 10.1175/jpo-d-15-0105.1

Zhou Xiangqian, Zhu Guoping, Hu Song. 2020. Influence of tides on mass transport in the Bransfield Strait and the adjacent areas, Antarctic. Polar Science, 23: 100506, doi: 10.1016/j.polar.2020.100506

Zilberman N V, Becker J M, Merrifield M A, et al. 2009. Model estimates of M_2 internal tide generation over mid-atlantic ridge topography. Journal of Physical Oceanography, 39(10): 2635–2651, doi: 10.1175/2008jpo4136.1